東北大学機関リポジトリ
TOUR
Tohoku University Repository
東北大学

Degenerate ground state in the classical pyrochlore antiferromagnet Na3Mn(CO3)2Cl

著者	Kazuhiro Nawa, Daisuke Okuyama, Maxim Avdeev, Hiroyuki Nojiri, Masahiro Yoshida, Daichi Ueta, Hideki Yoshizawa, Taku J Sato
journal or publication title	Physical Review B
volume	98
number	144426
page range	1-8
year	2018-10-18
URL	http://hdl.handle.net/10097/00125549

doi: 10.1103/PhysRevB.98.144426

Degenerate ground state in the classical pyrochlore antiferromagnet $Na_3Mn(CO_3)_2Cl$

Kazuhiro Nawa,[1,*] Daisuke Okuyama,[1] Maxim Avdeev,[2,3] Hiroyuki Nojiri,[4] Masahiro Yoshida,[5] Daichi Ueta,[5] Hideki Yoshizawa,[5] and Taku J. Sato[1]

[1]*Institute of Multidisciplinary Research for Advanced Materials, Tohoku University, 2-1-1 Katahira, Sendai 980-8577, Japan*
[2]*Australian Nuclear Science and Technology Organisation, Kirrawee DC, NSW 2232, Australia*
[3]*School of Chemistry, The University of Sydney, Sydney, NSW 2006, Australia*
[4]*Institute for Materials Research, Tohoku University, 2-1-1 Katahira, Sendai 980-8577, Japan*
[5]*Institute for Solid State Physics, The University of Tokyo, Kashiwa, Chiba 277-8581, Japan*

(Received 14 June 2018; revised manuscript received 1 October 2018; published 18 October 2018)

In an ideal classical pyrochlore antiferromagnet without perturbations, an infinite degeneracy in a ground state leads to the absence of magnetic order and a spin-glass transition. Here we present $Na_3Mn(CO_3)_2Cl$ as a new candidate compound where classical spins are coupled antiferromagnetically on the pyrochlore lattice and report its structural and magnetic properties. The temperature dependences of the magnetic susceptibility and heat capacity and the magnetization curve are consistent with those of an $S = 5/2$ pyrochlore lattice antiferromagnet with nearest-neighbor interactions of 2 K. Neither an apparent signature of a spin-glass transition nor magnetic order is detected in magnetization and heat capacity measurements or powder neutron diffraction experiments. On the other hand, antiferromagnetic short-range order of the nearest neighbors is evidenced by the Q dependence of the diffuse scattering which develops around 0.85 $Å^{-1}$. A high degeneracy near the ground state in $Na_3Mn(CO_3)_2Cl$ is supported by the magnetic entropy, estimated as almost 4 $J\,K^{-2}\,mol^{-1}$ at 0.5 K.

DOI: 10.1103/PhysRevB.98.144426

I. INTRODUCTION

Frustrated magnets have been receiving attention for decades since competing interactions destabilize conventional magnetic order and instead induce nontrivial magnetic order, quantum phases, and critical phenomena [1–5]. The classical pyrochlore magnet belongs to a class of the system that exhibits interesting magnetic properties [6–12]. For the pyrochlore magnet where *Ising* spins are coupled by *ferromagnetic* nearest-neighbor interactions, two-in/two-out ground states on a single tetrahedron lead to a highly degenerate ground state as a whole [12], which is called a spin-ice [13–15]. In the case of *Heisenberg* spins with *antiferromagnetic* nearest-neighbor interactions, the ground state is also highly degenerate, and moreover, ground-state manifolds can be transformed into each other by rotating spins without an energy change [9,10]. Thus, ideally, a classical Heisenberg pyrochlore antiferromagnet exhibits neither long-range magnetic order nor a spin-glass transition as $T \to 0$. However, such a large degeneracy can be easily lifted by small perturbations. For instance, a spin-glass state is induced by bond disorder between magnetic ions [16–18], a nematic state can occur from biquadratic interactions [19], and Néel order, partial order, and multi-Q magnetic orders from next-nearest-neighbor or third-nearest-neighbor interactions [20–23]. In real materials, these weak interactions often result in magnetic order or a spin-glass state. For instance, the representative pyrochlore antiferromagnet FeF_3 [24] exhibits an all-in/all-out magnetic order at $T_N = 15$-22 K [25,26], possibly due to the weak single-ion anisotropy [24] or coexisting Dzyaloshinskii Moriya and biquadratic interactions [27]. Some magnetic orders or spin-glass states are also found in other antiferromagnets with highly Heisenberg interactions, such as $Mn_2Sb_2O_7$ [24,28,29], $Gd_2Ti_2O_7$ [30–32], $ZnFe_2O_4$ [33,34], and $NaSrMn_2F_7$ [35].

In this paper, we report structural and magnetic properties of $Na_3Mn(CO_3)_2Cl$, a new Heisenberg antiferromagnet where classical spins are placed on a pyrochlore lattice. The crystal structure of $Na_3Mn(CO_3)_2Cl$ is shown in Fig. 1. It is a Mn analog of $Na_3Co(CO_3)_2Cl$: a pyrochlore network of magnetic ions is formed by TO_6 octahedra linked by carbonate ions (CO_3^{2-}) [36]. Although its crystal structure is not exactly identical to that of a pyrochlore structure (an ordered derivative of the fluorite structure), its magnetism should be equivalent to that of a pyrochlore antiferromagnet. For this reason, in the following we simply call both pyrochlore antiferromagnets. For $Na_3Co(CO_3)_2Cl$, several phase transitions are detected through macroscopic measurements and powder neutron-scattering experiments [37]. In particular, all-in/all-out magnetic order occurs as the temperature is decreased below $T_N = 1.5$ K. The coexistence of antiferromagnetic nearest-neighbor interactions J and weak ferromagnetic next-nearest-neighbor interactions J' may lead to successive magnetic transitions [37]. In addition, orbital degeneracy should also be a key since coupling between the orbital degeneracy and a spin-3/2 for Co^{2+} ($3d^7$) selects a Kramers doublet as the ground state. On the other hand, $Na_3Mn(CO_3)_2Cl$ consists of Mn^{2+} ($3d^5$), which should have little anisotropy because of the absence of orbital degeneracy. Thus, this compound is appropriate to

*knawa@tohoku.ac.jp

 ©2018 American Physical Society

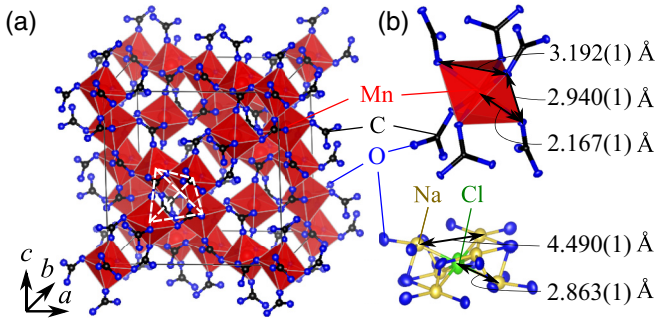

FIG. 1. Crystal structure of $Na_3Mn(CO_3)_2Cl$. Mn, C, O, Na, and Cl atoms are represented by red, black, blue, dark yellow, and green ellipsoids, reflecting the atomic displacement parameters of each atom. (a) Arrangement of MnO_6 octahedra in a unit cell. MnO_6 octahedra are connected by carbonate ions, forming a pyrochlore network of Mn atoms. One of the tetrahedrons forming the pyrochlore lattice is indicated by dashed white lines. Na and Cl atoms are omitted for clarity. (b) Local structures around Mn and Cl atoms. The VESTA program is used for visualization [38].

investigate the magnetic properties of a classical pyrochlore antiferromagnet experimentally. To examine the ground state of $Na_3Mn(CO_3)_2Cl$, we performed magnetization and heat capacity measurements and powder neutron diffraction experiments. We present these results in the following sections and discuss the magnetic properties of $Na_3Mn(CO_3)_2Cl$ as a classical pyrochlore antiferromagnet with a large degeneracy near the ground state.

II. EXPERIMENTS

The $Na_3Mn(CO_3)_2Cl$ sample was synthesized by a solvothermal method. First, 2 mmol of Na_2CO_3 (212.0 mg) and 1 mmol of $NaHCO_3$ (84.0 mg) were dissolved in 0.56 ml of pure water, and then 1 mmol of $MnCl_2 \cdot 4H_2O$ (197.9 mg) was added and the mixture was stirred until the solution became homogeneous. Next, 9 ml of ethanol and 2 mmol of 1,10-phenanthroline monohydrate (317.2 mg) were added, with 10 min stirring, after each procedure. The mixed solution was poured into a 25-ml-volume Teflon container together with a magnetic stirrer, sealed in a stainless vessel, and heated at 160°C for 4 days, with stirring at a speed of 150 rpm. After heat treatment, the solution was filtered, and the sample was further washed several times to remove extra carbonates, salts, and organic materials. For this purpose, both ethylene glycol and the mixed solution of pure water (2.24 ml) and ethanol (36 ml) were selected as solvents. An aggregate of brown octahedral crystals was left after the whole procedure.

The crystal structure was determined from a single-crystal synchrotron x-ray diffraction (XRD) experiment performed at BL-8A, Photon Factry KEK, using a 30-μm-long octahedral crystal. The energy of the incident beam was tuned to 12.4 keV ($\lambda = 0.9999$ Å) and scattered x rays were collected with a cylinder-shaped imaging plate. Nitrogen gas was flowed toward the crystal to avoid absorption of moisture and heated to keep the temperature to 300 K. An $|F|$ table down to a resolution limit of 0.5 Å was made through the RAPID-offline program (Rigaku), using anomalous scattering factors calculated relativistically [39]. The crystal structure was determined by a direct method using the SIR2004 program [40] and refined using the Crystals program.

TABLE I. Refinement parameters for $Na_3Mn(CO_3)_2Cl$. A full-matrix least-squares method on $|F|^2$ is adopted for the refinement.

2θ range for data collection	7.0°–144.5°
Index range	$-24 \leqslant h \leqslant 23$
	$-27 \leqslant k \leqslant 27$
	$-21 \leqslant l \leqslant 22$
Reflections collected	8766
Independent reflections	855
Completeness to θ	0.868[a]
Data/restraints/parameters	706/0/23
Goodness of fit on $\|F\|^2$	0.956
R indices for all data (R, R_w)	0.0136, 0.0247
Extinction coefficient	6.1(10)
Largest diff. peak and hole (eÅ^{-3})	0.35 and −0.39

[a]The completeness is lower than standard since a spindle axis is fixed and thus only a single-axis rotation is possible.

Physical properties were measured using several batches of the polycrystalline sample synthesized by the solvothermal method. Both dc- and ac-magnetic susceptibilities were measured with the Magnetic Properties Measurement System (Quantum Design), and the heat capacity was measured by a relaxation method using the Physical Properties Measurement System (Quantum Design). A low-temperature probe equipped with an adiabatic-demagnetization refrigerator was used to measure the magnetic susceptibility below 2 K [41]. The high-field magnetization curve was measured using a pulse magnet combined with a ^{3}He cryostat to reach down to 0.5 K. To investigate whether or not magnetic order is present at low temperatures microscopically, powder neutron diffraction measurements were performed at the high-resolution powder diffraction spectrometer ECHIDNA [42]. Neutrons with wavelength $\lambda = 2.4395$ Å were selected by a monochromator using Ge 331 reflections. Neutron diffraction patterns at 0.05 and 2 K were obtained using a dilution refrigerator. To improve the thermal conductivity, deuterated isopropanol (d-isopropanol) was put in a copper can together with 0.9 g of polycrystalline sample. In addition, neutron diffraction patterns were collected at 1.5–200 K from 1.3 g of polycrystalline sample set in a vanadium can, using a top-loading cryostat. Rietveld analysis was made by the Fullprof suite [43].

III. CRYSTAL STRUCTURE

Refinement and structural parameters determined from the single-crystal XRD analysis are summarized in Tables I and II, respectively. The crystal structure of $Na_3Mn(CO_3)_2Cl$ is shown in Fig. 1. Structural features of $Na_3Mn(CO_3)_2Cl$ are the same as those of $Na_3Co(CO_3)_2Cl$ [36,37]: TO_6 (T = Co, Mn) octahedra are connected by carbonate ions to form the pyrochlore lattice. In addition, local structures around Mn(Co) and Cl atoms are also quite similar. Mn atoms coordinate with six carbonate ions, forming MnO_6 octahedra

TABLE II. Structural parameters of $Na_3Mn(CO_3)_2Cl$ at 300 K determined from the single-crystal XRD experiment. The space group is $Fd\bar{3}$ (No. 203), and the lattice parameter is $a = 14.1932(3)$ Å. Atomic coordinations are represented by fractional coordinates. The anisotropic displacement parameters U_{11}, U_{22}, U_{33}, U_{12}, U_{13}, and U_{23} and equivalent isotropic displacement parameter B_{eq} [$B_{eq} = 8\pi^2/3 \times (U_{11} + U_{22} + U_{33})$] are listed in units of Å^2. Occupancy is fixed at 1 for all atoms.

	Site	x	y	z	U_{11}	U_{22}	U_{33}	U_{12}	U_{13}	U_{23}	B_{eq}
Na	48f	1/8	0.34864(2)	5/8	0.01663(10)	0.01788(11)	0.01907(11)	0	−0.00337(8)	0	1.410(4)
Mn	16c	0	1/2	1/2	0.00952(3)	0.00952(3)	0.00952(3)	−0.00043(2)	−0.00043(2)	−0.00043(2)	0.752(1)
C	32e	0.03054(2)	0.71946(2)	0.53054(2)	0.00864(7)	0.00864(7)	0.00864(7)	−0.00043(7)	0.00043(7)	−0.00043(7)	0.682(2)
O	96g	−0.02533(2)	0.65000(2)	0.51505(2)	0.01300(10)	0.01066(9)	0.01845(11)	−0.00377(7)	0.00011(8)	−0.00237(8)	1.108(3)
Cl	16d	1/4	1/4	1/2	0.02573(7)	0.02573(7)	0.02573(7)	0.01009(7)	−0.01009(7)	−0.01009(7)	2.032(2)

compressed trigonally along [111] or equivalent directions. The length of the Mn-O bond is 2.170 Å and quite close to the 2.190 Å in $MnCO_3$ [44], where Mn atoms are also linked with six carbonate ions. Cl atoms are characterized by a large and anisotropic atomic displacement parameter: in particular, it becomes large along [111] or equivalent directions, while it becomes small in the perpendicular direction. This feature indicates specific coordination around Cl atoms rather than a large deficiency of Cl atoms themselves. There are six Na atoms around Cl atoms with a bond length of 2.873 Å, which is a little larger than the 2.820 Å in NaCl [45]. In addition, a large distortion of Na_6Cl octahedra yields a large vacancy on [111] or equivalent directions, resulting in mobile Cl atoms. Consistency between single-crystal XRD and powder neutron diffraction experiments was confirmed by applying the Rietveld refinement method to the powder neutron diffraction patterns. Starting from initial parameters based on the crystal structure determined from the single-crystal XRD analysis, powder neutron diffraction patterns are well reproduced, with very little change of atomic positions (Fig. 2). The refined lattice constants are $a = 14.1353(1)$ and 14.1631(3) Å at 1.5 and 200 K, respectively. Several very weak peaks due to a $\lambda/2$ component are observed, which are included in the refinement. In addition, 1.8 wt% $MnCO_3$ is detected as an impurity phase. As the temperature is decreased from 200 to 1.5 K, a broad peak around 20° develops at low temperatures, indicating enhancement of antiferromagnetic correlations. Details are discussed in Sec. V.

IV. MAGNETIC AND THERMODYNAMIC PROPERTIES

The temperature dependence of the magnetic susceptibility is well explained by that of a $S = 5/2$ pyrochlore antiferromagnet, as shown in Fig. 3(a). At low fields, magnetic susceptibility exhibits an anomaly at 34 K, which is due to a ferrimagnetic transition of $MnCO_3$ included as the impurity phase [46]. To reduce the effect of the impurity phase, the following analysis is performed on the data measured at 1 T. As shown by the solid blue line in Fig. 3(a), the inverse susceptibility above 50 K well follows the Curie-Weiss law. From a fit of the magnetic susceptibility at 50–300 K to the Curie-Weiss law, the effective moment and a Weiss temperature are estimated as $\mu_{\rm eff}^2 = 35.6(1)$ and $\Theta_W = 40.9(1)$ K, respectively. The temperature-independent susceptibility is fixed at -1.23×10^{-4} cm^3 mol^{-1} from Pascal constants of the constituent atoms. The effective moment is consistent with 35 expected for $S = 5/2$ and an isotropic g value of 2. Below 50 K, the magnetic susceptibility becomes slightly lower than that expected from the Curie-Weiss law, which is consistent with that expected for a classical pyrochlore antiferromagnet. A similar temperature dependence is also observed in $Gd_2Ti_2O_7$ [30], while the magnetic susceptibility becomes larger than that expected from the Curie-Weiss law in $Mn_2Sb_2O_7$ [28,29] and $NaSrMn_2O_7$ [35]. The data at 10-300 K are well fitted by a [4, 4] Padé approximant applied to a high-temperature-series expansion of the $S = 5/2$ pyrochlore antiferromagnet [47]. The fit yields a nearest-neighbor interaction J and a g value of $J = 2.03(1)$ K and $g = 1.99(1)$, respectively.

At low temperatures, signatures of magnetic order and a spin-glass transition are not observed, as presented in Figs. 3(b) and 3(c). Figure 3(b) shows the magnetic susceptibility measured at 0.6–3 K using the adiabatic-demagnetization refrigerator. As the temperature decreases, the magnetic susceptibility slightly increases but does not show any anomaly which would suggest a magnetic transition. Figure 3(c) shows the ac magnetic susceptibility measured at

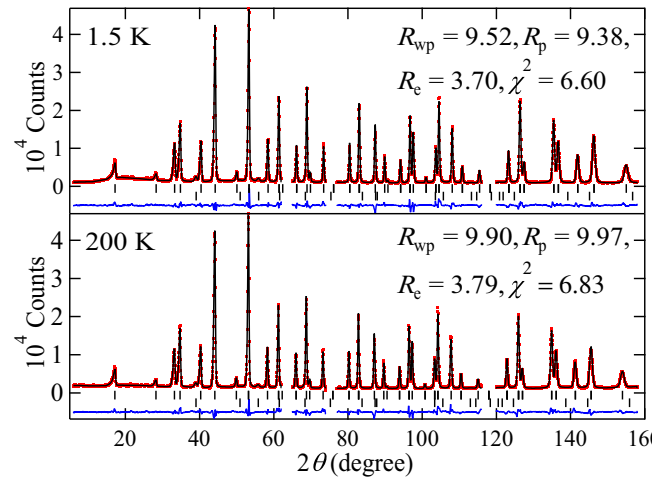

FIG. 2. Powder neutron diffraction pattern at 1.5 and 200 K collected by ECHIDNA together with Rietveld analysis. Total neutron counts are normalized by 1.5×10^6 ncu. Observed and calculated intensities and the difference between the intensities are shown by red points, black curves, and blue curves, respectively. Reflection positions for $Na_3Mn(CO_3)_2Cl$ and $MnCO_3$ expected at a wavelength of 2.4395 Å are indicated by the upper and lower vertical lines, respectively. Reflections from Al cryostats are removed from the figure.

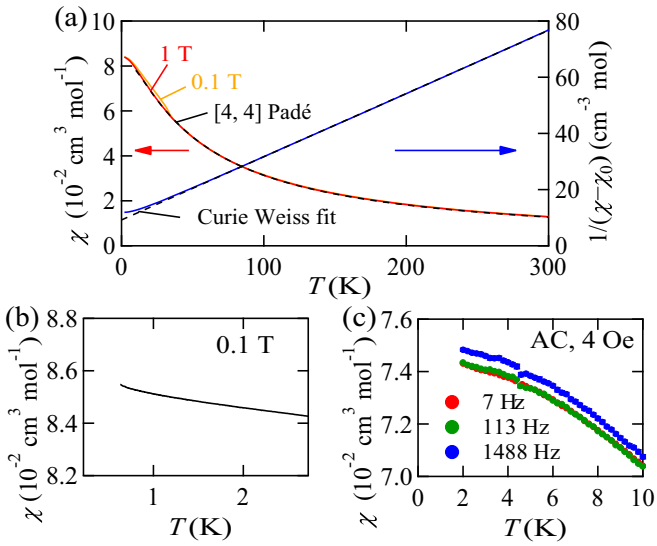

FIG. 3. (a) Temperature dependence of the magnetic susceptibility measured at 1 T (red curve) and 0.1 T (orange curve) with zero-field cooling. The blue curve indicates the inverse magnetic susceptibility. Dashed and dotted curves represent a fit to the [4, 4] Padé approximant for a high-temperature series expansion of a pyrochlore lattice [47] and a Curie-Weiss fit, respectively. (b) Magnetic susceptibility down to 0.6 K measured by the low-temperature probe after cooling in a field of 5 T that is then decreased to 0.1 T. (c) The ac susceptibility below 10 K.

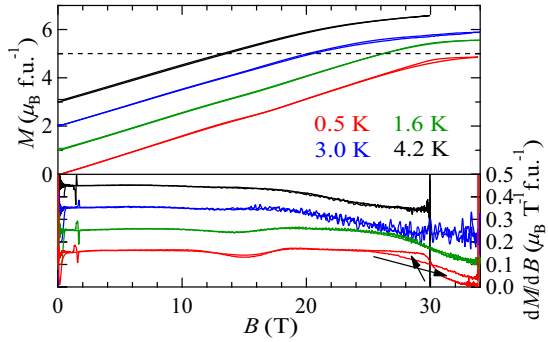

FIG. 4. Magnetization curves (top) and field derivative (bottom) measured at 0.5 K (red curve), 1.6 K (green curve), 3.0 K (blue curve), and 4.2 K (black curve). Curves measured at higher temperatures are shifted for clarity. Arrows indicate the time sequence of the magnetization process around a hysteresis loop.

2–10 K at frequencies of 7–1488 Hz. The jump observed at 4.5 K is not from the sample but due to the small instability of the temperature around the boiling point of helium. Spin-glass-like features such as the occurrence of a broad peak and the frequency dependence of its peak position are not observed in this frequency range.

High-field magnetization curves also provide a J consistent with that estimated from the magnetic susceptibility. Figure 4 shows high-field magnetization curves measured by a pulse field. At 0.5 K, the magnetization linearly increases with an increasing magnetic field as expected from a mean-field approximation: the sum of four spins on each tetrahedron and, thus, the total magnetization should be proportional to the magnetic field. The magnetization curve saturates at the saturation field B_s of 30.6(3) T. According to the mean-field approximation, the saturation field is related to J as $g\mu_B B_s = 8JS$, where μ_B represents the Bohr magnetron. Thus, from $B_s = 30.6$ T and $g = 1.99$ it can be roughly estimated as 2.0(1) K, which is consistent with the value estimated from the magnetic susceptibility. A hysteresis is present in the magnetization curve, which is due to a magnetocaloric effect: the temperature is increased (decreased) with an increasing (a decreasing) magnetic field under a quasiadiabatic condition because of the remaining degeneracy below the magnetic saturation. The slope of the magnetization curve near the magnetization saturation becomes smaller at higher temperatures, indicating smaller degeneracy at high fields. In addition, the slope of the magnetization curve slightly decreases at half-magnetization. The decrease becomes prominent at low temperatures, suggesting that the anomaly is not caused by an order-by-disorder mechanism. Instead, we speculate that small anisotropic interactions or weak spin-lattice couplings may be present. It is noted that spin-lattice couplings can stabilize three-up/one-down configurations for each tetrahedron under a magnetic field, leading to a 1/2 plateau in the magnetization curve [48,49]. For the magnetization curve of $Na_3Mn(CO_3)_2Cl$, the field range where the decrease in the slope is observed is limited to a width of about 3.5 T. This means that biquadratic interactions as small as 3% of J can be present if the spin-lattice couplings cause the anomaly in magnetization. Biquadratic interactions never stabilize the magnetic order [19], and thus its presence does not contradict the following discussion.

The temperature dependence of the heat capacity indicates a large degeneracy near the ground state. The temperature dependence of the heat capacity C is shown in Fig. 5(a). The heat capacity exhibits a broad peak at low temperatures, as is usual for pyrochlore antiferromagnets [29,30,35,37]. As shown in Fig. 5(b), the peak is slightly broadened at 7 T, indicating that frustration is partially relieved by the magnetic field. The total heat capacity measured at 10–25 K is fitted with the sum of the phonon and magnetic contributions: the former and the latter are estimated by the Debye model and a [4, 4] Padé approximant of the high-temperature series expansion [47], respectively. The fit is represented by the black curve in Fig. 5(a); note that it is shown only above 10 K since the approximant is not reliable below the temperature of $JS(S+1)/2$. The heat capacity at 10–25 K agrees well with the fitted curve. This fit yields a Debye temperature Θ_D of 334(5) K and nearest-neighbor interactions J of 2.0(1) K, which are consistent with magnetization measurements.

The magnetic contribution is extracted by subtracting the phonon contribution [blue curve in Fig. 5(a)], resulting in a temperature dependence of the magnetic heat capacity divided by the temperature, C_{mag}/T, which is shown as red circles in Fig. 5(c). As the temperature is further decreased, C_{mag}/T increases gradually down to 2 K. Below 2 K, C_{mag}/T increases greatly but never exhibits a peak which would indicate a magnetic transition, as shown in the inset in Fig. 5(c). In fact, this is consistent with the neutron diffraction experiments, which did not show an apparent signature of the magnetic order even at 0.05 K, as discussed later. Since the temperature

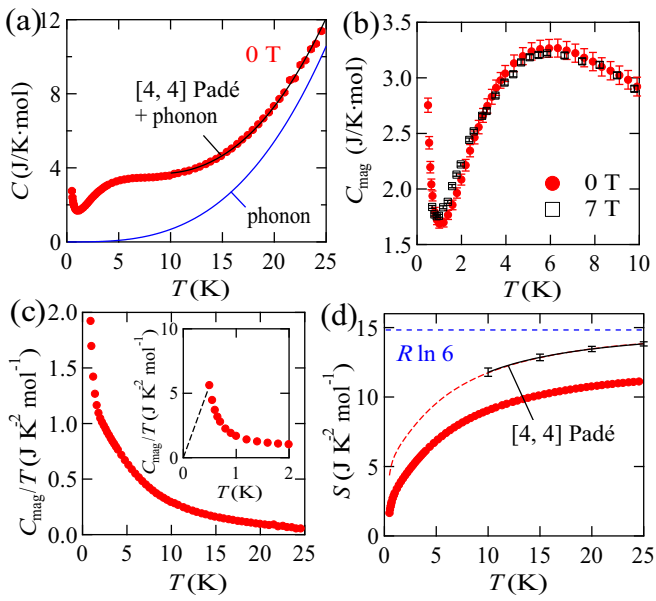

FIG. 5. (a) Temperature dependence of the heat capacity at 0 T. The solid black curve indicates the fit including both phonon and magnetic contributions, while the solid blue curve represents the phonon contribution estimated from the fit (see text for details). (b) Magnetic heat capacity at 0 T (filled circles) compared with that at 7 T (open squares). (c) Magnetic heat capacity divided by the temperature $C_{\rm mag}/T$ at 0 T. Inset: Enlarged view below 2 K. The dashed black line corresponds to the extension of $C_{\rm mag}/T$ below 0.5 K just for the estimation of the magnetic entropy. (d) Magnetic entropy determined from integrating $C_{\rm mag}/T$. The dashed black line in the inset in Fig. 5(c) leads to the estimate indicated by filled red circles. Dashed red curves are obtained by shifting the estimated entropy above so that they match the solid black curve, which indicates the magnetic entropy expected for a pyrochlore lattice with $J = 2.0$ K. The error bar for the solid black curve corresponds to an entropy difference of 0.2 K in J.

below 0.5 K was not accessible in the present experiment, $C_{\rm mag}/T$ is assumed to decrease linearly down to 0 as the dashed black curve in the inset in Fig. 5(c). Then the temperature dependence of the magnetic entropy is estimated as open black circles in Fig. 5(d). The solid black curve corresponds to the magnetic entropy of an $S = 5/2$ pyrochlore antiferromagnet with $J = 2.0 \pm 0.2$ K. It is estimated by integrating the $C_{\rm mag}/T$ derived from the [4, 4] Padé approximant between the temperature T and 2000 K and then subtracting the integrated value from the total entropy of $R \ln 6$. Because of the high consistency in the estimatation of J from magnetization and heat capacity measurements, the magnetic entropy should also follow that expected for a $S = 5/2$ pyrochlore antiferromagnet. However, the magnetic entropy estimated from the above assumption (red circles) is much smaller than that expected for the pyrochlore antiferromagnet (solid black curve). An offset should be added to the temperature dependence to compensate the underestimate of the magnetic entropy below 0.5 K, as shown by the dashed red curve. To achieve a good agreement, the magnetic entropy of more than $4\,{\rm J\,K^{-2}\,mol^{-1}}$, which corresponds to one-fourth of the total entropy, should persist at 0.5 K. A large degeneracy should be present near the ground state, as expected for classical pyrochlore antiferromagnets. Note that the heat capacity from nuclear spins, which can exhibit a strong Schottky anomaly, is neglected in the above discussion. The deficiency of the magnetic entropy above 0.5 K can be even larger if contributions from nuclear spins are not negligible.

V. NEUTRON DIFFRACTION EXPERIMENTS

The magnetization and heat capacity measurements reveal that the magnetic properties of $Na_3Mn(CO_3)_2Cl$ are well described by an $S = 5/2$ nearly Heisenberg pyrochlore antiferromagnet. In this section, we present results of the neutron diffraction experiments which evidence that a short-range order characteristic of a pyrochlore antiferromagnet develops below 50 K, while an apparent signature of the magnetic order is absent down to 0.05 K. Figure 2 represents neutron diffraction patterns measured at 1.5 and 200 K. As discussed in Sec. III, the neutron diffraction pattern at 1.5 K is well fitted by nuclear reflections. Only very weak unindexed peaks are left at 26.9° and 35.6°, which are likely from a small amount of impurities. While a large change in the peak intensity is often expected at a small 2θ angle if magnetic order occurs in a $S = 5/2$ system, such a large change was not observed. This is consistent with the absence of any anomalies in the magnetization and heat capacity measurements from the main phase. The atomic positions at 1.5 and 200 K determined from the Rietveld refinement are almost identical, supporting the validity of the refinements. To investigate whether or not magnetic order is present at much lower temperatures, the neutron diffraction pattern is collected at 0.05 K and compared with a 2 K pattern taken under the same condition as shown in Fig. 6(a). In spite of the presence of additional Bragg peaks from d-isopropanol, which is used as the heat conduction medium in the sample can, the diffraction patterns at 0.05 and 2 K do not show any additional peaks up to $2\theta = 70°$. Note that $Na_3Co(CO_3)_2Cl$ exhibits all-in-all-out order at 1.5 K, evidenced by heat capacity and neutron diffraction experiments [37]. Even if all-in-all-out order is present, the upper limit on the moment size would be $0.5\,\mu_B$ according to the experimental error around 022 reflections. This is only 10% of the $5\,\mu_B$ expected for Mn^{2+} ions and unreasonably small for a nearly classical system. This clearly indicates that the magnetic order should be largely suppressed owing to magnetic frustration in $Na_3Mn(CO_3)_2Cl$.

Although no strong magnetic Bragg peaks are found, a small change in the intensity is observed at low scattering angles. Figure 7 represents the intensities at low scattering angles plotted as a function of the scattering wave vector Q. The background determined from empty can measurements and the intensities of nuclear reflections estimated by the Rietveld refinement (Fig. 2) are subtracted. As the temperature is decreased, a broad peak develops at $0.85\,{\rm \AA}^{-1}$, indicating the development of antiferromagnetic short-range order. The development persists down to very low temperatures, as indicated by the intensity difference shown in Fig. 6(b). To investigate its origin, we calculated neutron-scattering cross sections using the mean-field approximation [7,50–52], which is useful for simply estimating approximate exchange constants. To avoid confusion, we use the same notations as in Ref. [52]. A

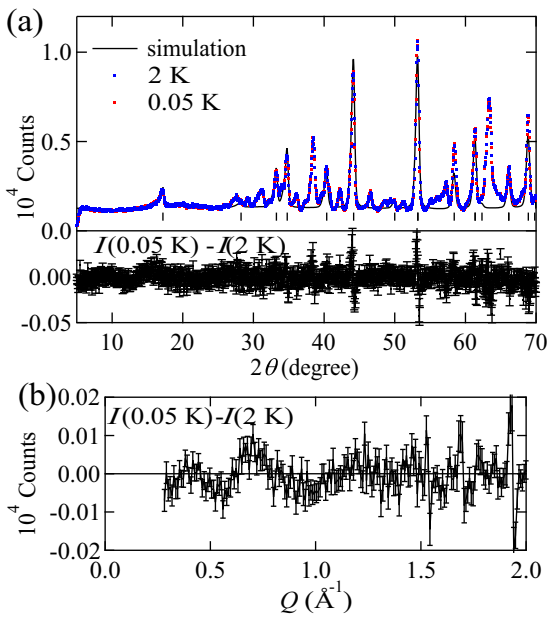

FIG. 6. (a) Neutron powder diffraction patterns measured at 0.05 K (red points) and 2 K (blue points) compared with simulated patterns (black points). Total neutron counts are normalized by 6.0×10^5 ncu. Vertical black lines indicate the positions of nuclear reflections. The lower panel indicates the intensity difference between the data at 0.05 K and those at 2 K. (b) Intensity difference between the data at 0.05 K and those at 2 K as a function of Q. Data points are binned to improve the statistics.

pyrochlore lattice is regarded as a face-centered cubic lattice with four sublattices in each unit cell. The positions of the ith Bravais lattice point and ath sublattice in every unit cell are denoted $\mathbf{R}_i$ and $\mathbf{r}^a$, respectively. The relative position from the bth sublattice in the jth Bravais lattice to the ath sublattice in the ith Bravais lattice is defined as $\mathbf{R}_{ij}^{ab} \equiv \mathbf{r}^a + \mathbf{R}_i - \mathbf{r}^b - \mathbf{R}_j$. A unit vector along the $\mu = x$, y, or z direction is represented by $\mathbf{n}^\mu$.

First, Fourier transformations of nearest-neighbor (NN), next-nearest neighbor (NNN), and dipolar interactions (denoted J, J', and $D_{\rm dd}$, respectively) are summed up for each sublattice and x, y, and z component, resulting in a 12×12 matrix,

$$\begin{aligned} J_{\mu\nu}^{ab}(\mathbf{q}) = &- J \sum_i \delta_{ab:\mathrm{NN}} (\mathbf{n}^\mu \cdot \mathbf{n}^\nu) \exp\bigl(-i\mathbf{q}\cdot\mathbf{R}_{ij}^{ab}\bigr) \\ &- J' \sum_i \delta_{ab:\mathrm{NNN}} (\mathbf{n}^\mu \cdot \mathbf{n}^\nu) \exp\bigl(-i\mathbf{q}\cdot\mathbf{R}_{ij}^{ab}\bigr) \\ &+ D_{\rm dd} \sum_i \left(\frac{\mathbf{n}^\mu \cdot \mathbf{n}^\nu}{|\mathbf{R}_{ij}^{ab}|^3} - \frac{3\bigl(\mathbf{n}^\mu \cdot \mathbf{R}_{ij}^{ab}\bigr)\bigl(\mathbf{n}^\nu \cdot \mathbf{R}_{ij}^{ab}\bigr)}{|\mathbf{R}_{ij}^{ab}|^5} \right) \\ &\times R_{\rm NN}^3 \exp\bigl(-i\mathbf{q}\cdot\mathbf{R}_{ij}^{ab}\bigr), \end{aligned} \tag{1}$$

which is defined for every wave vector $\mathbf{q}$ in the first Brillouin zone. $R_{\rm NN}$ is the distance of the nearest-neighbor interactions. Note that the signs of J, J', and $D_{\rm dd}$ are opposite those in Ref. [52] since we defined the antiferromagnetic exchange to be positive. The Kronecker delta is included in Eq. (1) to take the sum only between nearest or next-nearest neighbors. The lattice sum of dipolar interactions is treated via the Ewald summation method [52–55].

From $\lambda_\mu^\alpha(\mathbf{q})$ and eigenstates $\mathbf{U}_\mu^\alpha(\mathbf{q})$ ($\alpha = 1, 2, 3, 4$ and $\mu = x'$, y', z' represent normal modes) of the matrix, the mean-field neutron-scattering cross section can be estimated by

$$\begin{aligned} \frac{d\sigma(\mathbf{Q})}{d\Omega} &= \frac{C}{3}\{f(Q)\}^2 \sum_{\alpha,\mu} \frac{\bigl|\mathbf{F}_{\mu\perp}^\alpha(\mathbf{q})\bigr|^2}{1 - \lambda_\mu^\alpha(\mathbf{q})/(3T)}, \\ \mathbf{F}_{\mu\perp}^\alpha(\mathbf{q}) &\equiv \sum_a \bigl\{\mathbf{U}_\mu^{\alpha,a}(\mathbf{q}) - \bigl(\mathbf{U}_\mu^{\alpha,a}(\mathbf{q})\cdot\mathbf{Q}\bigr)\mathbf{Q}\bigr\} \exp(i\mathbf{G}\cdot\mathbf{r}^a), \\ \mathbf{U}_\mu^{\alpha,a}(\mathbf{q}) &= \sum_u \mathbf{n}^u U_{\mu,u}^{\alpha,a}(\mathbf{q}) = \sum_u \mathbf{n}^u U_{u,\mu}^{*a,\alpha}(\mathbf{q}), \end{aligned} \tag{2}$$

where $U_{u,\mu}^{a,\alpha}$ is an (a, u) component of $\mathbf{U}_\mu^\alpha$, $\mathbf{Q}$ is related to the reciprocal wave vector $\mathbf{G}$ as $\mathbf{Q} = \mathbf{q} + \mathbf{G}$, and C and $f(Q)$ denote an arbitrary coefficient and a magnetic form factor, respectively. In the mean-field approximation, correlation functions are regarded as the sum of a zeroth-order term of self-correlations and a first-order term proportional to the inverse temperature [7,52]. This rough approximation is not valid at low temperatures, since the mean-field neutron-scattering cross section diverges at $T_{\rm C}$, which is defined by the maximum of $\lambda_\mu^\alpha(\mathbf{q})/3$ among all α, μ, and $\mathbf{q}$. This disadvantage does not matter for the following discussion of the Q dependence, though it makes the temperature variation of the cross section unreliable. Thus, C is used as an adjustable parameter which varies with the temperature for each fit. In addition, a constant temperature-independent background which best reproduces the 1.5 K scan is also added in the fit.

The neutron diffraction patterns are compared with the powder average of the scattering cross section estimated from Eq. (2), as presented in Fig. 7. The solid curve represents a fit to the J-$D_{\rm dd}$ pyrochlore model. In the fit, J is fixed at 2 K, estimated from magnetization measurements, J' is fixed at 0, and $D_{\rm dd}$ is set to -0.125 K, estimated from dipolar interactions expected for Mn^{2+} ($5\,\mu_{\rm B}$). This simple model, with only one fitting parameter T, well reproduces the broad peak due to antiferromagnetic nearest-neighbor interactions J; the effect of the dipolar interactions $D_{\rm dd}$ is small. An antiferromagnetic J yields a scattering cross section which extends between $\mathbf{Q} = (0, 0, 2)$ and (1,1,2), and $\mathbf{Q} = (1, 1, 0)$ and (2,2,0). The fit is also performed by the J-J'-$D_{\rm dd}$ pyrochlore model, as indicated by the dashed curve in Fig. 7. Introducing a ferromagnetic J' in addition to J and $D_{\rm dd}$ slightly sharpens the peak. This is because it induces the energy minimum of the ground state at $\mathbf{q} = (h, h, 0)$ ($h \sim 3/4$) [22,23], and thus the scattering cross section at $\mathbf{Q} = (h, h, 2)$ and $(2 - h, 2 - h, 0)$ is increased. The best fit is achieved when J' is weakly ferromagnetic, -0.4 K. A weakly ferromagnetic J' is also suggested for $Na_3Co(CO_3)_2Cl$ [37]. As shown in Fig. 7, Q dependence measured at high temperatures is also well reproduced by both models. For the J-$D_{\rm dd}$ pyrochlore model the transition temperature becomes $T_{\rm C}^{\rm MF} = 1.5$ K according to the mean-field theory, and the fit yields temperatures of $T/T_{\rm C}^{\rm MF} = 1.7$, 2.3, 6.0, and 14 for the 1.5, 10, 50, and 200 K data, respectively. On the other hand, the J-J'-$D_{\rm dd}$ pyrochlore model leads to $T_{\rm C}^{\rm MF} = 2.0$ K, and the fit yields temperatures of $T/T_{\rm C}^{\rm MF} = 1.6$, 2.2, 4.5, and 10 for the 1.5, 10, 50, and 200 K data, respectively. It is difficult to conclude whether or not

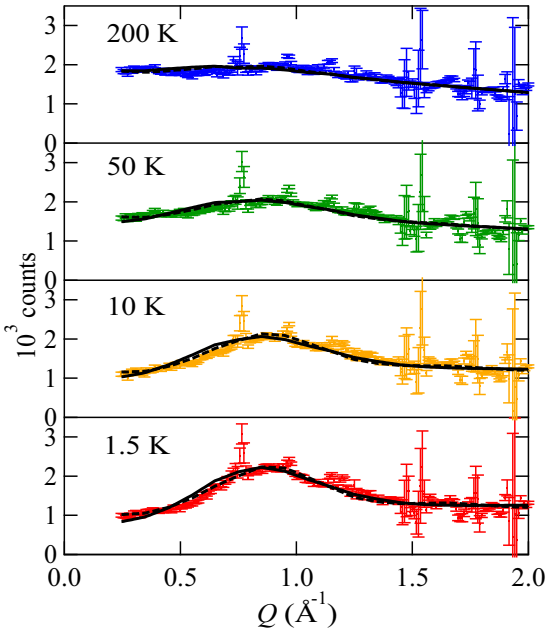

FIG. 7. Q dependence of the intensity measured at 1.5, 10, 50, and 200 K. Data points are binned to improve the statistics. Total counts are normalized by 1.5×10^6 ncu. Solid and dashed curves represent the fit for a pyrochlore antiferromagnet with NN interactions ($J = 2$ K) and that for a pyrochlore antiferromagnet with NN and NNN interactions ($J = 2$ K, $J' = -0.4$ K), respectively.

a ferromagnetic J' is present only from the two fits because of their small difference. However, it is more likely that next-nearest-neighbor interactions J' are very small, since magnetic order is likely to be absent above 0.05 K. The transition temperature to the multi-Q order increases with increasing next-nearest-neighbor interactions J' according to the Monte Carlo simulations [22,23]. If a J' of -0.4 K is present, multi-Q order should appear near 2 K.

As discussed in previous and the present section, the magnetic properties of $Na_3Mn(CO_3)_2Cl$ are consistent with those of a classical pyrochlore antiferromagnet. The temperature dependence of the magnetic susceptibility and heat capacity, the magnetization curve, and the Q dependence of the diffuse scattering are well explained by those of the pyrochlore antiferromagnet. In addition, the magnetization, heat capacity, and neutron diffraction patterns exhibit no apparent signature of a spin-glass transition above 2 K or magnetic order above 0.05 K. Furthermore, the estimation of the magnetic entropy indicates a large degeneracy near the ground state. From these features, it is likely that $Na_3Mn(CO_3)_2Cl$ is a good candidate for a classical nearly Heisenberg pyrochlore antiferromagnet; extra interactions which lift the ground-state degeneracy should be small. Single-ion or exchange anisotropies should be absent from $Na_3Mn(CO_3)_2Cl$, while they may lead to the all-in/all-out order in $Na_3Co(CO_3)_2Cl$ [37]. In addition, small dipole interactions cannot lift the line degeneracy along the (111) directions [30]. It should be noted that the possibility of a spin-glass transition below 2 K is small from the thorough consistency. To reveal the spin dynamics in this compound, low-energy excitations should be further examined by neutron-scattering, NMR, or μSR experiments.

VI. SUMMARY

The magnetic properties of $Na_3Mn(CO_3)_2Cl$ are investigated by means of magnetization, heat capacity, and neutron diffraction experiments. The temperature dependence of the magnetic susceptibility and the magnetization curve are consistent with those of a $S = 5/2$ pyrochlore lattice antiferromagnet with nearest-neighbor interactions. The neutron diffraction patterns indicate the development of antiferromagnetic short-range order below 50 K. No apparent signature of a spin-glass transition or magnetic order is observed above 2 or 0.05 K, respectively. A large degeneracy should remain near the ground state, as indicated by the heat capacity measurement; the magnetic entropy of 4 J K^{-2} mol^{-1} remains at 0.5 K. In this sense, $Na_3Mn(CO_3)_2Cl$ should exhibit an interesting disordered ground state as expected for a classical pyrochlore antiferromagnet.

ACKNOWLEDGMENTS

We thank H. Sagayama for support with the single-crystal x-ray diffraction experiment, S. Asai and T. Masuda for help with heat capacity measurements, and T. Hiraiwa and K. Yamauchi for fruitful discussions. This work was partly supported by a Grant-In-Aid for Scientific Research (Grant No. 17K18744) from MEXT of Japan, the CORE Laboratory Research Program "Dynamic Alliance for Open Innovation Bridging Human, Environment and Materials" of the Network Joint Research Center for Materials and Devices, and the Motizuki Fund of Yukawa Memorial Foundation. High-field magnetization and heat capacity measurements were carried out under the Inter-University Cooperative Research Program of the Institute for Materials Research, Tohoku University, and the Visiting Researcher's Program of the Institute for Solid State Physics, University of Tokyo, respectively. Synchrotron x-ray diffraction experiments were performed with the approval of the Photon Factory Program Advisory Committee (No. 2016G143). Travel expenses for the experiment on ECHIDNA at ANSTO were partly sponsored by the General User Program of ISSP-NSL, University of Tokyo.

[1] G. Misguich and C. Lhuillier, in *Frustrated Spin Systems*, edited by H. T. Diep (World Scientific, Singapore, 2005), p. 229.
[2] A. P. Ramirez, Annu. Rev. Mater. Sci. **24**, 453 (1994).
[3] J. E. Greedan, J. Mater. Chem. **11**, 37 (2001).
[4] L. Balents, Nature **464**, 199 (2010).
[5] L. Savary and L. Balents, Rep. Prog. Phys. **80**, 016502 (2017).
[6] P. W. Anderson, Phys. Rev. **102**, 1008 (1956).
[7] J. N. Reimers, A. J. Berlinsky, and A.-C. Shi, Phys. Rev. B **43**, 865 (1991).
[8] J. N. Reimers, Phys. Rev. B **45**, 7287 (1992).
[9] R. Moessner and J. T. Chalker, Phys. Rev. Lett. **80**, 2929 (1998).
[10] R. Moessner and J. T. Chalker, Phys. Rev. B **58**, 12049 (1998).

[11] J. S. Gardner, M. J. Gingras, and J. E. Greedan, Rev. Mod. Phys. **82**, 53 (2010).
[12] S. T. Bramwell and M. J. Harris, J. Phys.: Condens. Matter **10**, L215 (1998).
[13] M. J. Harris, S. T. Bramwell, D. F. McMorrow, T. Zeiske, and K. W. Godfrey, Phys. Rev. Lett. **79**, 2554 (1997).
[14] A. P. Ramirez, A. Hayashi, R. J. Cava, R. B. Siddharthan, and S. Shastry, Nature **399**, 333 (1999).
[15] S. T. Bramwell and M. J. P. Gingras, Science **294**, 1495 (2001).
[16] L. Bellier-Castella, M. J. P. Gingras, P. C. W. Holdsworth, and R. Moessner, Can. J. Phys. **79**, 1365 (2001).
[17] T. E. Saunders and J. T. Chalker, Phys. Rev. Lett. **98**, 157201 (2007).
[18] A. Andreanov, J. T. Chalker, T. E. Saunders, and D. Sherrington, Phys. Rev. B **81**, 014406 (2010).
[19] N. Shannon, K. Penc, and Y. Motome, Phys. Rev. B **81**, 184409 (2010).
[20] D. Tsuneishi and H. Kawamura, J. Phys.: Condens. Matter **19**, 145273 (2007).
[21] T. Nakamura and D. Hirashima, J. Magn. Magn. Mater. **310**, 1297 (2007).
[22] G.-W. Chern, R. Moessner, and O. Tchernyshyov, Phys. Rev. B **78**, 144418 (2008).
[23] T. Okubo, T. H. Nguyen, and H. Kawamura, Phys. Rev. B **84**, 144432 (2011).
[24] J. N. Reimers, J. E. Greedan, C. V. Stager, M. Bjorgvinnsen, and M. A. Subramanian, Phys. Rev. B **43**, 5692 (1991).
[25] G. Ferey, R. Depape, M. Leblanc, and J. Pannetier, Rev. Chim. Miner. **23**, 474 (1986).
[26] J. N. Reimers, J. E. Greedan, and M. Björgvinsson, Phys. Rev. B **45**, 7295 (1992).
[27] A. Sadeghi, M. Alaei, F. Shahbazi, and M. J. P. Gingras, Phys. Rev. B **91**, 140407(R) (2015).
[28] H. D. Zhou, C. R. Wiebe, A. Harter, N. S. Dalal, and J. S. Gardner, J. Phys.: Condens. Matter **20**, 325201 (2008).
[29] D. C. Peets, H. Sim, M. Avdeev, and J.-G. Park, Phys. Rev. B **94**, 174431 (2016).
[30] N. P. Raju, M. Dion, M. J. P. Gingras, T. E. Mason, and J. E. Greedan, Phys. Rev. B **59**, 14489 (1999).
[31] J. D. M. Champion, A. S. Wills, T. Fennell, S. T. Bramwell, J. S. Gardner, and M. A. Green, Phys. Rev. B **64**, 140407(R) (2001).
[32] J. R. Stewart, G. Ehlers, A. S. Wills, S. T. Bramwell, and J. S. Gardner, J. Phys.: Condens. Matter **16**, L321 (2004).
[33] W. Schiessl, W. Potzel, H. Karzel, M. Steiner, and G. M. Kalvius, A. Martin, M. K. Krause, I. Halevy, J. Gal, W. Schäfer, G. Will, M. Hillberg, and R. Wäppling, Phys. Rev. B **53**, 9143 (1996).
[34] K. Kamazawa, Y. Tsunoda, H. Kadowaki, and K. Kohn, Phys. Rev. B **68**, 024412 (2003).
[35] M. B. Sanders, J. W. Krizan, K. W. Plumb, T. M. McQueen, and R. J. Cava, J. Phys.: Condens. Matter **29**, 045801 (2016).
[36] Y. Zheng, A. Ellern, and P. Kögerler, Acta Crystallogr. Sec. C **67**, i56 (2011).
[37] Z. Fu, Y. Zheng, Y. Xiao, S. Bedanta, A. Senyshyn, G. G. Simeoni, Y. Su, U. Rücker, P. Kögerler, and T. Brückel, Phys. Rev. B **87**, 214406 (2013).
[38] K. Momma and F. Izumi, J. Appl. Crystallogr. **44**, 1272 (2011).
[39] D. T. Cromer and D. Liberman, J. Chem. Phys. **53**, 1891 (1970).
[40] M. C. Burla, R. Caliandro, M. Camalli, B. Carrozzini, G. L. Cascarano, L. De Caro, C. Giacovazzo, G. Polidori, D. Siliqi, and R. Spagna, J. Appl. Crystallogr. **40**, 609 (2007).
[41] T. J. Sato, D. Okuyama, and H. Kimura, Rev. Sci. Instrum. **87**, 123905 (2016).
[42] K.-D. Liss, B. Hunter, M. Hagen, T. Noakes, and S. Kennedy, Physica B (Amsterdam) **385–386**, 1010 (2006).
[43] J. Rodriguez-Carvajal, Physica B (Amsterdam) **192**, 55 (1993).
[44] H. Effenberger, K. Mereiter, and J. Zemann, Z. Kristallogr. **156**, 233 (1981).
[45] H. E. Swanson and R. K. Fuyat, *Standard X-Ray Diffraction Patterns*, National Bureau of Standards Circular, No. 359 (National Bureau of Standards, 1953), Vol. 2, pp. 41–43.
[46] A. S. Borovik-Romanov, Sov. Phys. JETP **9**, 539 (1959).
[47] H.-J. Schmidt, A. Lohmann, and J. Richter, Phys. Rev. B **84**, 104443 (2011); A. Lohmann, H.-J. Schmidt, and J. Richter, *ibid.* **89**, 014415 (2014).
[48] K. Penc, N. Shannon, and H. Shiba, Phys. Rev. Lett. **93**, 197203 (2004).
[49] D. L. Bergman, R. Shindou, G. A. Fiete, and L. Balents, Phys. Rev. B **74**, 134409 (2006).
[50] J. N. Reimers, Phys. Rev. B **46**, 193 (1992).
[51] H. Kadowaki, Y. Ishii, K. Matsuhira, and Y. Hinatsu, Phys. Rev. B **65**, 144421 (2002).
[52] M. Enjalran and M. J. P. Gingras, Phys. Rev. B **70**, 174426 (2004).
[53] P. P. Ewald, Ann. Phys. (Leipzig) **64**, 253 (1921).
[54] M. Born and K. Huang, *Dynamical Theory of Crystal Lattices*, (Oxford University Press, London, 1968), p. 248.
[55] S. L. de Leeuw, J. W. Perram, and E. R. Smith, Proc. R. Soc. London A **373**, 27 (1980).